ACS EARTH AND SPACE CHEMISTRY

http://pubs.acs.org/journal/aesccq

Article

Photocatalytic Oxidation of Dissolved Mn^{2+} by TiO_2 and the Formation of Tunnel Structured Manganese Oxides

Haesung Jung, Colin Snyder, Wenqian Xu, Ke Wen, Mengqiang Zhu, Yan Li, Anhuai Lu, and Yuanzhi Tang*

Cite This: *ACS Earth Space Chem.* 2021, 5, 2105−2114

Read Online

ACCESS | Metrics & More | Article Recommendations | Supporting Information

ABSTRACT: The redox reaction of manganese (Mn) is of great environmental, geological, and public health significance, as Mn oxides control the distribution and electron flow of numerous nutrients and contaminants in natural and engineered environments. Current understanding on the oxidation pathways of Mn(II) to Mn(III/IV) mainly focuses on biotic processes due to their much higher oxidation rates than those of abiotic processes. This study demonstrates rapid photocatalytic oxidation of Mn^{2+}(aq) under circumneutral conditions catalyzed by naturally abundant semiconducting TiO_2 minerals. Notably, the photocatalytic oxidation rates are comparable to or even higher than those of reported biotic/abiotic processes. In addition, the rapid photocatalytic oxidation leads to the formation of large tunnel structured Mn oxides (todorokite and romanechite) on the surface of TiO_2. These findings suggest that photocatalytic oxidation of Mn^{2+}(aq) by natural semiconducting minerals is likely an important yet previously overlooked pathway for understanding the occurrence of natural Mn oxide coatings on rock surfaces. In addition, considering the increasing input of photoreactive engineered nanoparticles into environmental systems, this study shows the potential impacts of nanoparticles on influencing natural redox cycles.

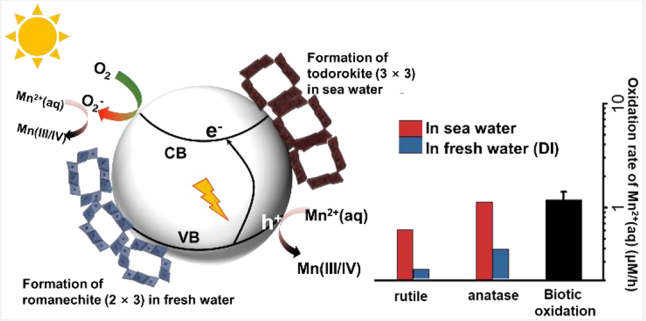

KEYWORDS: *Mn oxides, Ti oxide, nanoparticles, photochemistry, oxidation, tunnel structure*

1. INTRODUCTION

Mn(III/IV) (oxyhydr)oxides (hereafter Mn oxides) are a group of ubiquitous natural minerals in terrestrial and aquatic settings. They play important roles in numerous elemental cycles and affect the electron flow in nature.[1−9] They have high reduction potential ($E_{MnO_2/Mn^{2+}} \sim 500$ mV at pH 7)[10] and high specific surface area (around 10−200 m^2/g),[11,12] and are among the most reactive minerals and the most significant solid oxidants in nature. Thus, understanding the redox reactions of Mn in terristrial, freshwater, and high-salinity aqueous systems (e.g., seawater) has been considered a key for understanding the geochemical electron cycles in the history of Earth and Mars.[13−16] With their high redox reactivity and adsorption capacity, Mn oxides are also widely used in energy and environmental engineering systems for energy storage, water treatment, and contaminant removal.[17−21] For example, recent studies demonstrated the application of Mn oxides for harvesting energy from wastewater and salinity gradient[22,23] as well as for the degradation of antimicrobial agents, organic contaminants, and heavy metals.[23−28]

Because of the important roles that Mn oxides play in natural and engineered systems, many studies have explored the kinetics and mechanisms of their formation and transformation, as well as redox reactions involving Mn oxides. Previous studies showed that the abiotic homogeneous oxidation of Mn^{2+}(aq) by molecular oxygen is kinetically sluggish and takes years even though it is thermodynamically favorable.[29,30] Mineral surface catalyzed heterogeneous oxidation of Mn^{2+}(aq) by molecular oxygen takes 5−2,800 days (half-life) under circumneutral conditions.[29,31] In contrast, microbially mediated processes via enzymes (e.g., multicopper oxidase) or reactive oxygen species (ROS; such as superoxide) show much faster oxidation (1−69 days half-life).[31−34] Because of the widespread presence of Mn-oxidizing microorganisms and the fast oxidation rate, biotic processes have been generally accepted as the most significant contributor to the oxidation of Mn^{2+}(aq) and formation of Mn oxides in natural low-temperature environments. Interestingly, recent studies showed that photochemically generated superoxide by dissolved organic matter or nitrate can also enable indirect photooxidation of Mn^{2+}(aq) (i.e., oxidation of Mn^{2+}(aq) by

Received: May 23, 2021
Revised: July 15, 2021
Accepted: July 26, 2021
Published: August 9, 2021

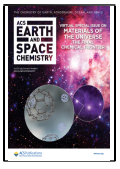

https://doi.org/10.1021/acsearthspacechem.1c00154
ACS Earth Space Chem. 2021, 5, 2105−2114

photochemically generated oxygen-related species) at rates comparable to biotic processes.[35−39] These exciting results shed lights on the potentially overlooked contribution of photochemistry, an abiotic process, to the oxidation of Mn^{2+}(aq) and formation of Mn oxides.

Notably, previously known biotic/abiotic processes typically lead to the formation of highly disordered and poorly crystalline layered Mn oxides (LMOs) that are structurally similar to vernadite (δ-MnO_2) or hexagonal birnessite. Although diverse tunnel structured Mn oxides (TMOs) occur ubiquitously in many environmental settings,[40] the detailed mechanisms of their formation have not been clearly resolved in laboratory studies under circumneutral conditions. Most studies showed the transformation of LMO to TMO under pH or temperature conditions significantly deviating from low-temperature circumneutral conditions.[41−44] In our recent study under circumneutral pH and ambient temperature condition, we demonstrated redox cycling driven transformation of LMO to TMO.[45] However, although this study provided a new angle for understanding the transformation of LMO to TMO under fluctuating natural conditions such as those at oxic/anoxic interfaces, direct formation of TMO from the oxidation of Mn^{2+}(aq) was rarely observed under laboratory conditions and its feasibility and mechanism remain a puzzle.

Natural semiconducting minerals (such as metal oxides and sulfides) are widespread in nature and capable of direct redox reactions at conduction or valence band via photoexcitation.[46] Although evidence for the direct heterogeneous photocatalysis of Mn^{2+}(aq) (i.e., oxidation through the electron transfer from Mn^{2+}(aq) to valence band of natural semiconducting mineral) is lacking, it is thermodynamically feasible as the valence band position of many natural minerals is higher than the reduction potential of Mn(III/IV)/Mn^{2+}(aq). Thus, a photoexcited hole in a valence band is thermodynamically feasible to oxidize Mn^{2+}(aq). A recent observation on the photon-to-electron conversion by natural semiconducting minerals on rock surfaces supports the potential of mineral photocatalysis and the subsequent direct photocatalytic oxidation of Mn^{2+}(aq) by natural semiconducting minerals.[47] A recent study described the oxidation of Mn^{2+}(aq) on natural semiconducting minerals (Fe and Ti oxides), but the high concentration of Mn^{2+}(aq) (14 mM) used in the study was not representative of natural conditions.[48] Systematic studies are thus desired to further explore the reaction kinetics and mechanisms of mineral catalyzed photocatalytic oxidation of Mn^{2+}(aq) under environmentally relevant conditions, as well as the structure of the formed Mn oxides.

In natural systems, one of the most photoreactive semiconducting minerals is TiO_2. Ti is the ninth most abundant element in Earth's crust, and rutile is the most commonly occurring structure of natural TiO_2.[49] Anatase is a polymorph of TiO_2.[50,51] Due to their strong photoreactivity, both rutile and anatase nanoparticles are used extensively in photocatalytic energy and environmental applications.[46,51−53] Because of the widespread anthropogenic use of TiO_2 in the past two decades, many studies have reported rapidly increasing concentrations of engineered TiO_2 nanoparticles in surface waters and wastewater treatment systems.[53−57] While extensive studies have been conducted to evaluate the toxicity of TiO_2 nanoparticles in nature, their photocatalytic effects on natural redox cycles remains elusive. Thus, investigating the roles of TiO_2 minerals in the photocatalytic oxidation of Mn^{2+} and formation of Mn oxides have important implications for both natural and engineered systems.

In this study, we show rapid photocatalytic oxidation of Mn^{2+}(aq) in the presence of rutile and anatase (representing natural minerals and emerging engineered nanoparticles of TiO_2, respectively). The observed oxidation rates are comparable to or even faster than currently known biotic processes. In addition, we show that the direct formation of TMO with large tunnel size, such as todorokite (3 × 3) and romanechite (2 × 3), occurs via heterogeneous nucleation on the surface of TiO_2. Considering the abundance of natural semiconducting minerals, our findings confirm the importance of direct photocatalytic oxidation for explaining the oxidation of Mn(II) and the formation and diversity of Mn oxides in environmental systems. These results also point to the potential influence of environmental nanoparticles on natural element and electron cycles.

2. EXPERIMENTAL SECTION

Materials and Reagents. Rutile and anatase TiO_2 phases were obtained from Alfa Aesar and were confirmed phase pure by X-ray diffraction (XRD). Their specific surface areas were measured by using Brunauer−Emmett−Teller (BET) method with N_2 gas adsorption (Autosorb-1-MP surface pore analyzer, Quantachrome Corp.) and are 5.5 m^2/g for rutile and 51.5 m^2/g for anatase. $MnCl_2$ stock solution was used to prepare reaction solutions with 100 μM Mn^{2+}(aq) in artificial seawater (ASW) and deionized water (DI). In addition to 100 μM $MnCl_2$, the ASW contains 0.42 M NaCl, 0.025 M $MgSO_4$, 0.0091 M $CaCl_2$, 0.0089 M KCl, and 0.0024 M $NaHCO_3$.[58] The pH value of the ASW experiments remained at 7.9 ± 0.1 during the 8 h reaction without any adjustment. The pH value in the DI experiments was initially adjusted to 7.5 ± 0.1 and later adjusted every hour using dilute NaOH or HCl. Throughout the reaction, pH stayed within the range of 7.5−7.8. TiO_2 particles (0.1 g/L) were dispersed in 180 mL of ASW or DI solutions and sonicated for 10 min before starting the photocatalytic reactions. To understand the effect of cations on the rapid photocatalytic oxidation and formation of tunnel structured Mn oxides, parallel experiments were conducted by reacting anatase particles in DI water containing only one cation (0.42 M NaCl, 0.025 M $MgSO_4$, or 0.0091 M $CaCl_2$; consistent with their corresponding concentrations in ASW). The suspension pH was initially adjusted to 7.5 ± 0.1 and was adjusted every hour. It stayed within the range of 7.5−7.8 throughout the experiments. These experiments are referred to as single cation experiments.

Photocatalytic Oxidation of Mn^{2+}(aq). Photochemical experiments were initiated by illuminating the prepared TiO_2 suspension by a 450 W Xe-arc lamp light source (Newport). The light passed through a 10 cm IR water filter to avoid the increase of temperature. We used a borosilicate reactor with a quartz window (1 in. diameter) facing the light. The reaction suspension was magnetically stirred over the entire reaction process. Aliquots (0.3 mL) of the suspension were taken every hour to analyze the concentration of oxidized Mn(III,IV) using the leucoberbelin blue (LBB; Sigma-Aldrich) colorimetric method at 625 nm on an UV−vis spectrophotometer (Cary 60, Agilent). Calibration of the LBB method used $KMn^{VII}O_4$.[59] Because 1 mol of Mn(VII) oxidizes 5 mol of LBB, using the obtained calibration with Mn(VII), the amount of oxidized Mn^{2+} can be converted to Mn(III) or Mn(IV) equivalent by considering the oxidation state of Mn oxides. For example, 10

https://doi.org/10.1021/acsearthspacechem.1c00154
ACS Earth Space Chem. 2021, 5, 2105−2114

μM Mn(VII) is equivalent to 25 μM Mn(IV) or 50 μM Mn(III). Because it is difficult to accurately determine the oxidation state of the photochemically formed Mn oxides, we used Mn(III) equivalent calculation in order to compare the electron flow under different reaction conditions. All experiments were conducted in replicates.

Several control experiments were also conducted by using anatase in ASW, as this system showed the fastest oxidation among all tested conditions. (1) Dark experiments were conducted to differentiate photocatalytic oxidation (i.e., Mn(II) oxidation by photochemically generated holes) from mineral surface catalyzed oxidation (i.e., heterogeneous Mn(II) oxidation by molecular oxygen on a mineral surface[60,61]). (2) To determine the photoactive wavelength region of anatase for Mn^{2+}(aq) oxidation, a 400 or 550 nm optical cutoff filter (Newport) was used to cutoff lights lower than 400 or 550 nm wavelength, respectively. The optical filter was placed between the light source and reactor. Because anatase showed much higher oxidation rate as compared to rutile, the control experiment was conducted using anatase to clearly distinguish the effective wavelength region for the photocatalytic oxidation of Mn^{2+}(aq) by TiO_2. (3) Because TiO_2 can generate superoxide upon photoexcitation,[51] to confirm the contribution of superoxide for the oxidation of Mn^{2+}(aq), scavenge experiments were conducted by adding 0.1 μM superoxide dismutase (SOD; Sigma Aldirch) in the suspension to scavenge superoxide during the reaction. (4) A control experiment was conducted in the absence of TiO_2, which showed no oxidation of Mn^{2+}(aq) in both ASW and DI water conditions.

Calculation of Quantum Yield. Using the photocatalytic oxidation of Mn^{2+}(aq) by TiO_2 with 450 W Xe-arc lamp, we calculated the quantum yields of rutile and anatase in ASW and DI. Multiplying irradiance of 450 W Xe-arc lamp (Supporting Information Figure S1), wavelength, unit conversion factor, and absorbance at each wavelength provides photons generated by a certain wavelength of 450 W Xe-arc lamp light. The exposed area and penetration depth were multiplied in the reactor. To obtain total photons generated by anatase or rutile by 450 W Xe-arc lamp, the calculated number of photons per wavelength using eq 1 was integrated from 250 to 800 nm (Table S4).

$$I\left(\frac{\text{photons}}{\text{nm}\cdot\text{s}}\right) = \{I\ (\text{W}/(\text{cm}^2\cdot\text{nm})\}\{\text{wavelength (nm)}\} \times \{5.035 \times 10^{15}\ \text{photons}/(\text{s}\cdot\text{nm})\} \times \{\text{Abs}\ (1/\text{cm})\}\{\text{penetration depth (cm)}\} \times \{\text{area}\ (\text{cm}^2)\} \quad (1)$$

We used the concentration of Mn(III) equivalent, which represents successfully transferred holes from TiO_2. Because the Mn(III) equivalent concentration reached a plateau after 6 h for reaction in rutile suspension, we used the concentration at 6 h for the calculation of quantum yield.

$$\text{QY}\ (\%) = \frac{\text{total oxidized } Mn^{2+}\text{(aq) for 6 h}}{\text{total generated photons from } TiO_2 \text{ for 6 h}} \times 100 \quad (2)$$

Using the obtained quantum yields of TiO_2 in ASW and DI, we obtained the estimated oxidation rates of Mn^{2+}(aq) by TiO_2 under natural sunlight exposure. The spectrum of natural sunlight (reference E-490-00; Figure S1) is obtained from the National Renewable Energy Laboratory. Using eq 1 and integration, the total number of photons were obtained under sunlight irradiation. By multiplying the total number of photons and quantum yield, we obtained the estimated concentration of Mn(III) equivalent under sunlight irradiation in 6 h reaction. The oxidation rates under sunlight condition were estimated by linearizing the Mn(III) equivalent concentration between 0 and 6 h.

Characterization of Heterogeneously Nucleated Mn Oxides on TiO_2. At each time point, the reacted suspension was syringe filtered (0.2 μm) and analyzed by LBB colorimetric method to quantify the amount of Mn oxides formed on the surface of TiO_2 (heterogeneous nucleation) and in the solution (homogeneous nucleation). To identify the phases and oxidation states of Mn oxides, reacted solids were collected at the end of photocatalysis by repeated centrifugation and rinsing by DI water, followed by freeze-drying. The dried samples were analyzed using X-ray photoelectron spectroscopy (XPS), synchrotron XRD (SXRD), and synchrotron X-ray absorption spectroscopy (XAS), as detailed below.

Mn 3p XPS spectra, which show better sensitivity of the Mn oxidation state than Mn 2p spectra,[62,63] were obtained on a K-alpha XPS system with monochromatic Al Kα radiation (1486.6 eV) (ThermoFisher Scientific). Although Mn 3s spectra are also useful for analyzing the Mn oxidation state, the use of Mn 3s in this study was inappropriate due to its overlap with Mg 1s spectra for ASW samples. Energy calibration used C 1s spectra (284.6 eV). Fitting of Mn 3p spectra was conducted with allocations of Mn(II), Mn(III), and Mn(IV) at 47.8, 48.6, and 49.8 eV, respectively.

SXRD was measured at Beamline 17-BM-B (51.324 keV, λ = 0.24157 Å) at the Advanced Photon Source (APS, Lemont, IL, USA). Mn K-edge X-ray absorption spectroscopy (XAS) analysis was conducted at Beamline 4-1 at the Stanford Synchrotron Radiation Lightsource (SSRL, Menlo Park, CA, USA), Beamline 12-BM-B at APS, and Beamline 6-BM at National Synchrotron Light Source-II (NSLS-II, Upton, NY, USA). Both XANES (X-ray absorption near-edge structure) and EXAFS (extended X-ray absorption fine structure) data were collected. The monochromators were detuned by 40% to avoid higher order harmonics. Energy calibration used Mn foil. Multiple scans (2−6) were collected for each sample, averaged, and normalized for further analysis. Analysis of the Mn XANES spectra for each sample showed no evidence of photoreduction under the X-ray beam.

XAS data analysis was performed using the programs SIXPACK[64] and Ifeffit.[65] Linear combination fitting (LCF) of the Mn XANES region was conducted to determine the relative percentages of Mn(II), Mn(III), and Mn(IV) species and the average oxidation state (AOS) following previous procedures.[66] To obtain statistically meaningful fitting results, all possible combinations were fitted with at most four references among 12 references in Table S1. Among the obtained 781 different fitting results, 30 fitting results with the lowest R factors were selected and averaged to determine AOS and percentages of Mn valence states. Considering the typical 10% error for LCF, values lower than 5% were considered negligible. Details on the reference compounds and results for LCF analysis are in Table S1 and Table S2, respectively.

3. RESULTS AND DISCUSSION

Rapid Photocatalytic Oxidation of Mn^{2+}(aq). In the presence of TiO_2 minerals, Mn^{2+}(aq) in both ASW and DI was

https://doi.org/10.1021/acsearthspacechem.1c00154
ACS Earth Space Chem. 2021, 5, 2105−2114

quickly oxidized (Figure 1). The oxidation rates with different mineral phases and aqueous conditions (1.4−8.0 μM h^{-1}; Figure S2) are all comparable to or faster than those of biotic processes (~1.2 ± 0.2 μM h^{-1}).[37,67−69] This finding suggests that photocatalytic oxidation of Mn^{2+}(aq) by TiO_2 is a feasible scenario in nature due to the abundance of natural semiconducting TiO_2 minerals[49] and increasing concentrations of anthropogenic nanoparticles in environmental systems.[53−57,70] Indiscernible oxidation under dark condition indicates that both surface catalyzed oxidation of Mn^{2+}(aq) by TiO_2 (i.e., heterogeneous oxidation) and homogeneous oxidation of Mn^{2+}(aq) by dissolved oxygen in solutions are negligible compared to photocatalytic oxidation (Figure S3). Anatase shows about two times faster oxidation rates than rutile in both ASW and DI (Figure 1 and Figure S2). One might consider that such difference is due to the higher specific surface area of anatase (51.5 m^2 g^{-1}) than rutile (5.5 m^2 g^{-1}). However, surface area normalized concentrations of Mn(III) equivalent showed that the oxidized Mn^{2+}(aq) is about an order of magnitude higher in the presence of rutile than that of anatase (Figure S4), indicating that surface area is not the dominant controlling factor for the higher oxidation rates in anatase suspensions. This suggests that the higher oxidation rates in anatase suspensions is likely due to the higher photoreactivity of anatase for redox reaction.[51]

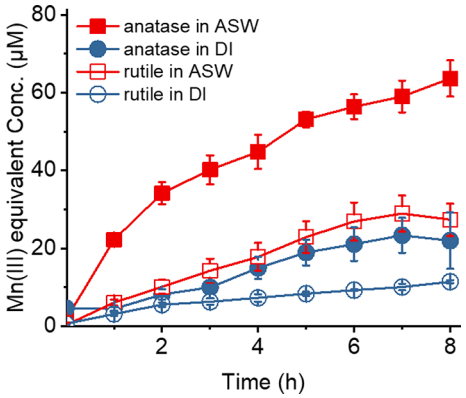

Figure 1. Rapid photocatalytic oxidation of Mn^{2+}(aq) by anatase and rutile in artificial seawater (ASW) and deionized (DI) water.

Except for the photocatalytic oxidation of Mn^{2+}(aq) in ASW-anatase suspension, all other conditions showed slowed oxidation after 6 h (Figure 1). This is possibly due to the gradual aggregation of TiO_2 particles, attachment of TiO_2 particles to the photochemical reactor, or blockage of surface active sites by the nucleated Mn oxide.

Interestingly, both anatase and rutile show faster oxidation in ASW than in DI. We considered that the pH difference in ASW (7.9 ± 0.1) vs DI (7.5−7.8) might partially contribute to the difference in oxidation rate. However, our thermodynamic calculations using Visual MINTEQ showed no significant changes in Mn(II) aqueous speciation in ASW and DI conditions (data not shown). Thus, we hypothesize that the difference in oxidation rate is likely due to the presence of high concentrations of cations (e.g., Na^+, K^+, Ca^{2+}, and Mg^{2+}) in ASW that can facilitate the oxidation of Mn^{2+}(aq) and formation of Mn oxides.[44,71,72] This is confirmed by the single cation experiments using solutions containing only one cation at the corresponding ASW concentration (i.e., 0.091 M Ca^{2+}, 0.025 M Mg^{2+}, or 0.420 M Na^+). The photocatalytic oxidation of Mn^{2+}(aq) by anatase in single cation experiments with Mg^{2+} (~8.2 μM h^{-1}) or Ca^{2+} (~6.6 μM hr^{-1}) (Figure S5A) shows oxidation rates similar to that of ASW systems (8.0 ± 0.6 μM h^{-1}). Interestingly, in the single cation experiment with Na^+, we observed the highest oxidation rate (~11.3 μM hr^{-1}) among all tested conditions. This indicates the profound role of cations in the photocatalytic oxidation and formation of Mn oxides on TiO_2 particles. The different phase of Mn oxides formed in the single cation experiments (Figure 2) also supports the influence of cations on the Mn oxide structure, as discussed below. Since this study focuses on the photocatalytic

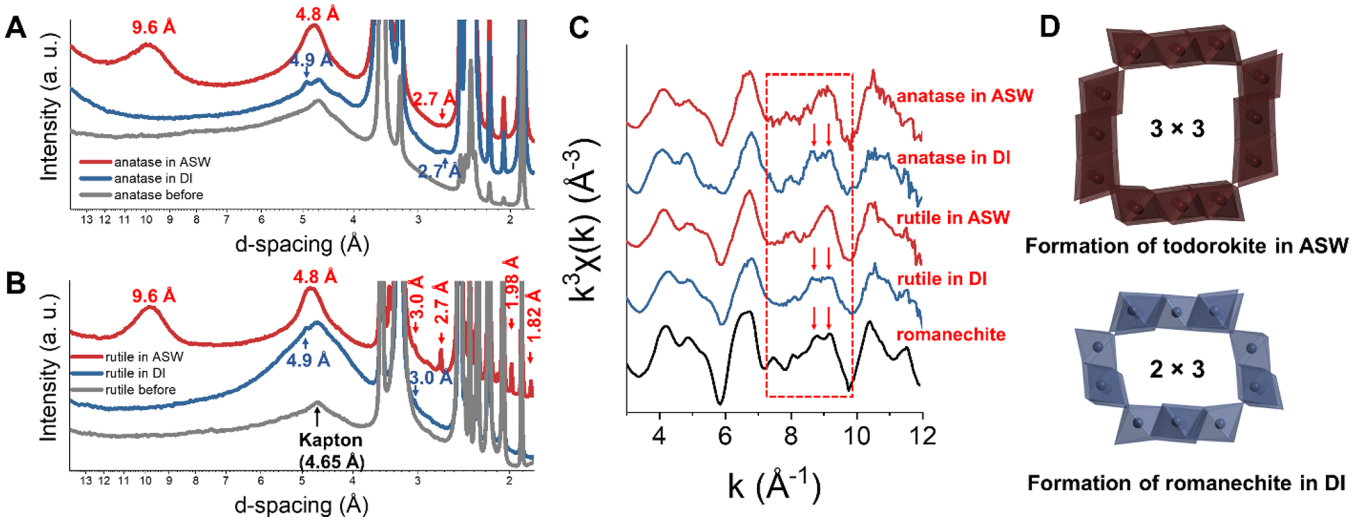

Figure 2. Formation of large tunnel structured Mn oxides on the surface of TiO_2. (A and B) Synchrotron XRD analyses show that the nucleated Mn oxide on the surface of both anatase and rutile in ASW is todorokite (3 × 3 tunnel structure). In DI system, weak diffraction occurred at 4.9 Å. Because several tunnel structured Mn oxides (romanechite (2 × 3), hollandite (2 × 2), and todorokite (3 × 3)) have diffraction peaks at this position, it is challenging to identify the phase of Mn oxide using SXRD alone. (C) EXAFS analysis confirms that Mn oxides formed in the DI system are structurally similar to romanechite. (D) Schematic structures are shown for todorokite (3 × 3 tunnel size) and romanechite (2 × 3 tunnel size).

https://doi.org/10.1021/acsearthspacechem.1c00154
ACS Earth Space Chem. 2021, 5, 2105−2114

oxidation of Mn^{2+}(aq) by TiO_2 nanoparticles and consequent formation of TMO, detailed mechanistic understanding of the roles of cations and anions in the oxidation rate is beyond the scope of this work. Further studies are warranted to explain the photocatalytic reactions of TiO_2 under varied aqueous conditions.

Formation of Large Tunnel Structured Mn Oxides. The rapid photocatalytic oxidation of Mn^{2+}(aq) led to the formation of Mn oxides on the surface of TiO_2. Mn(III,IV) species were not detected by the LBB method in the filtrate of the reaction suspensions at all times (Figure S3). Considering that homogeneously nucleated Mn oxides are 6−30 nm in diameter,[73] which can readily pass through 0.22 μm filters, the absence of Mn oxides in the filtrate indicates the high likelihood of heterogeneous nucleation of Mn oxides on the surface of TiO_2 instead of homogeneous nucleation of Mn oxide nanoparticles in solution.

Interestingly, we also observed the formation of TMO with large tunnels under all reaction conditions (Figure 2A,B). Considering that LMOs (such as δ-MnO_2 and birnessite) are the typical phases of homogeneously nucleated Mn oxides through biotic/abiotic processes,[36,37,74] the formation of TMOs in our system also strongly suggests the heterogeneous nucleation of Mn oxides on TiO_2 through photocatalytic oxidation of Mn^{2+}(aq). SXRD analyses of the 8 h samples in anatase-ASW and rutile-ASW suspensions (Figure 2A,B) indicate the formation of todorokite (3 × 3 tunnel size) with diffraction peaks at 9.6 and 4.8 Å d-spacing. Although the large d-spacing can also occur from buserite, which has similar structure to birnessite but with a 10 Å interlayer spacing, the interlayer of buserite (10 Å interlayer spacing) collapses to birnessite (~7 Å interlayer spacing) upon dehydration due to weakly bound interlayer H_2O in the interlayer positions.[40,75,76] Thus, the large d-spacing of our fully dehydrated samples (obtained under vacuum freeze-drying for 1 day) indicates that the nucleated Mn oxide on TiO_2 in ASW is todorokite. In anatase-DI and rutile-DI suspensions, SXRD showed only weak diffraction at ~4.9 Å, which occurs from all large tunnel structured Mn oxides (3 × 3, 3 × 2, and 2 × 2 tunnel size) (Figure 2A,B). To further identify the structure of the Mn oxides formed in DI experiments, we conducted Mn K-edge EXAFS analysis and identified the formation of romanechite-like structure (2 × 3 tunnel size; Figure 2C). Specifically, the region between 7 and 10 $Å^{-1}$ in k space is a well-known "indicator region" for Mn oxide structure.[77,78] In this region, Mn oxides formed in DI experiments have two peaks at ~8.7 and 9.2 $Å^{-1}$, consistent with the spectra of romanechite and distinctively different from the spectra of todorokite formed in ASW (Figure 2C) and hollandite (2 × 2 tunnel size; Figure S6). These results indicate an important observation that heterogeneous nucleation on natural mineral surfaces can facilitate the direct formation of TMO with large tunnels. Specifically, todorokite is one of the most ubiquitous natural Mn oxides, yet its formation in low-temperature environments is poorly constrained due to the difficulties in synthesizing this phase in laboratory settings through the transformation of LMO to TMO. Most previous studies employed reaction conditions that do not represent circumneutral low-temperature environments, such as the transformation of Mg^{2+}-intercalated LMO using reflux or hydrothermal reactions at temperatures above 100 °C.[41,42,44] Our findings suggest that photocatalytically promoted direct heterogeneous nucleation of Mn oxides on natural minerals might be an alternative pathway for explaining the formation of todorokite. In our system, the underlying TiO_2 minerals serve as templates to facilitate the heterogeneous nucleation of Mn oxides, which might have lowered the structural strain and formation energy for TMO. In addition, this observation also suggests a new phase selection pathway (i.e., formation of TMO via heterogeneous nucleation of Mn oxides) as compared to previously observed common formation of LMO induced by homogeneous nucleation of Mn oxides upon Mn(II) oxidation.[36,37,74] Future microscopic studies are warranted to further investigate the mechanism, structure, and morphology of the heterogeneously nucleated TMO, such as the use of high-resolution transmission electron microscopy (HRTEM) to analyze the micromorphology, potential presence of poorly crystalline LMO, and relationships with the mineral substrate.

Prior studies showed the importance of Mn(III) and large cations (e.g., Mg^{2+} and Ca^{2+}) on the transformation of LMO to TMO with large tunnels.[41,42,44,71,79−81] In our system, Mn oxides produced from all tested conditions contain considerable amounts of structural Mn(III) as probed by XPS and XANES (Figures 3 and S7 and Table S2), which is necessary to form TMO. The results show that Mn oxides formed in the presence of anatase have more Mn(III) in the structure than those formed in the rutile system. Specifically, Mn oxides formed in the anatase-ASW suspension show a higher content of Mn(III) than those formed in rutile-ASW suspension based on the fitting of Mn 3p XPS spectra. This feature can be readily observed from the lower peak position of Mn 3p spectra of the anatase-ASW sample than that of rutile-ASW (Figure 3). It is worth noting that obtaining accurate ratios of Mn(III/IV) using XPS and XANES is challenging, due to errors resulting from data fitting and the intrinsic differences of these techniques (i.e., XANES obtains bulk information whereas XPS detects near-surface structure).[82] Nonetheless, linear

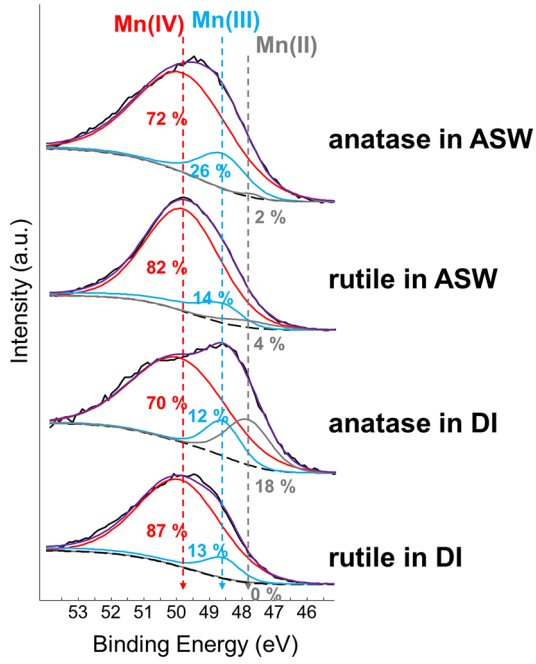

Figure 3. Mn 3p XPS spectra of Mn oxides formed on the surface of TiO_2. Fitting results show that all of the Mn oxides formed under varied conditions have Mn(III). Mn oxides formed in the presence of anatase have more Mn(III) than those formed in the rutile system.

https://doi.org/10.1021/acsearthspacechem.1c00154
ACS Earth Space Chem. 2021, 5, 2105−2114

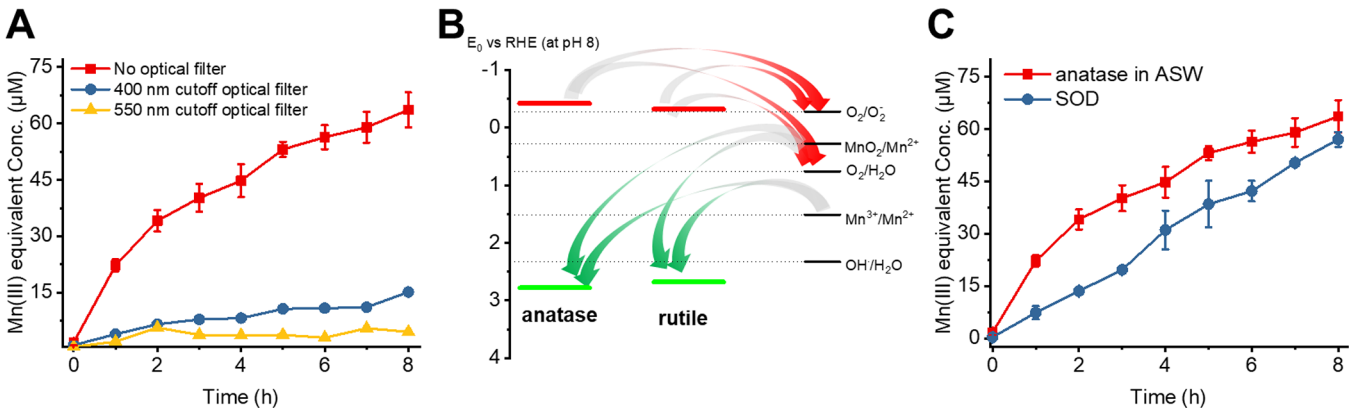

Figure 4. Mechanistic understanding of the photocatalytic oxidation of Mn^{2+}(aq) in the presence of TiO_2. (A) Control tests with 400 or 550 nm optical cutoff filters suggest that the rapid photocatalytic oxidation of Mn^{2+}(aq) with TiO_2 occurs from the photoexcited electron−hole pair mainly at wavelength < 400 nm. (B) The positions of valence and conduction bands show that the photocatalytic oxidation of Mn^{2+}(aq) with TiO_2 is thermodynamically feasible via both direct electron transfer and indirect reaction of Mn^{2+}(aq) with photocatalytically generated superoxide. (C) The decrease of oxidation rate in the presence of superoxide dismutase (SOD; a superoxide scavenger) indicates that both superoxide and photoexcited holes contribute to the rapid oxidation of Mn^{2+}(aq) in the presence of TiO_2 and light. In addition, the occurrence of superoxide indicates that oxygen is the electron acceptor, which enables the rapid direct electron transfer from Mn^{2+}(aq) to a hole in the valence band of TiO_2 by blocking the recombination of electron−hole pair.

combination fitting (LCF) of Mn XANES spectra also shows that the nucleated Mn oxides in anatase-ASW suspension have a higher content of Mn(III) than those formed in rutile-ASW suspension (Figure S7 and Table S2). Despite the difference in Mn(III) content, the Mn oxides formed in both anatase and rutile suspensions have the same structure (i.e., todorokite in ASW and romanechite in DI).

Interestingly, although the Mn oxides formed in rutile-DI and rutile-ASW suspensions show similar Mn(III) contents, they have different structures. This suggests that the observed difference in tunnel size between ASW (todorokite, 3 × 3) and DI (romanechite, 2 × 3) systems was likely resulted from the presence of cations in ASW, not from the difference in Mn(III) content. Indeed, results from the single cation experiments (DI water containing only Mg^{2+}, Ca^{2+}, or Na^{+} at their corresponding ASW concentrations) support the importance of cations in ASW in mediating the TMO formation. Among all anatase-single cation experiments (Mg^{2+}, Ca^{2+}, or Na^{+}), the Mn oxides produced in Mg^{2+} experiment show the most relevant structure to Mn oxide formed in anatase-ASW suspension, as revealed by linear combination fitting of Mn K-edge EXAFS spectra (Figure S5B and Table S3). This observation is consistent with prior studies showing the necessity of Mg^{2+} intercalation into LMO to enable the hydrothermal transformation of LMO to todorokite.[41,42,44,71,79−81] Ca^{2+} also likely contributes to the formation of todorokite, based on the similarity of the EXAFS indicator region for Mn oxides produced in the Ca^{2+} single cation experiment as compared to todorokite spectra. We can rule out the contribution of Na^{+} on the formation of todorokite in ASW based on the formation of romanechite-like structure (Figure S5B and Table S3). Overall, results from the single cation experiments indicate that, regardless of the mineral catalyst, large cations (e.g., Mg^{2+} and Ca^{2+}) in ASW are the main factors responsible for the structural difference during heterogeneous nucleation of Mn oxide on TiO_2 in ASW vs DI water. Detailed mechanistic investigation on the effects of cations on the oxidation of Mn^{2+}(aq) and the structure of nucleated Mn oxides is beyond the scope of this study and warrants further work.

Reaction Mechanisms. Our mechanistic study further reveals that photoexcitation of TiO_2 enables the rapid oxidation of Mn^{2+}(aq) by the generation of holes at valence band (direct oxidation) as well as superoxide (indirect oxidation), as explained below.

For Mn^{2+} oxidation by the generated holes at valence band (direct oxidation), we conducted parallel experiments using different optical cutoff filters in the anatase-ASW suspension, which shows the fastest oxidation, to elucidate the mechanisms of photocatalytic oxidation of Mn^{2+}(aq). We found that rapid oxidation occurs via the photoexcitation of electrons and holes from anatase (Figure 4A). Specifically, in the presence of 400 nm cutoff optical filter (which cuts off wavelengths at <400 nm), the oxidation of Mn^{2+}(aq) is significantly suppressed. This indicates that the rapid oxidation of Mn^{2+}(aq) occurs mainly from the photoexcitation in UVA region (320−400 nm), which matches the band gap of anatase (3.2 eV). With 550 nm cutoff optical filter (cutoff < 550 nm), little oxidation of Mn^{2+}(aq) occurred (Figure 4A) due to completely suppressed photoexcitation.

For Mn^{2+} oxidation by superoxide (indirect oxidation), TiO_2 is capable of generating superoxide because its conduction band is located at lower reduction potential than that of oxygen (O_2)/superoxide (O_2^-) (Figure 4C). Prior studies show that superoxide can readily oxidize Mn^{2+}(aq), while hydroxyl radical and hydrogen peroxide cannot.[36,68] In our control experiment with superoxide scavenger SOD, both the extent and rate of Mn^{2+} oxidation decreased slightly, indicating the contribution of superoxide (produced from photocatalysis) in the indirect oxidation of Mn^{2+} (Figure 4D). However, considering the small decrease in Mn^{2+} oxidation caused by SOD as compared to those caused by the cutoff filters (Figure 4D), direct electron transfer from Mn^{2+}(aq) to photogenerated holes is still considered as the dominant oxidation mechanism. In addition, the occurrence of superoxide and the observed direct electron transfer from Mn^{2+}(aq) to a hole in the valence band of TiO_2 indicate that oxygen is the electron acceptor which suppresses the recombination between the photogenerated electrons and holes.

https://doi.org/10.1021/acsearthspacechem.1c00154
ACS Earth Space Chem. 2021, 5, 2105−2114

4. ENVIRONMENTAL IMPLICATIONS

To assess the relative importance of this photocatalytic oxidation process in nature, we compare the oxidation rates obtained from this study to previously observed representative oxidation rates. Using the experimentally obtained photocatalytic oxidation rate, spectra of 450 W Xe-arc lamp and natural sunlight, and calculating the quantum yields (Table S4 and Figure S1), we extrapolated the laboratory oxidation rates obtained using 450 W Xe lamp to natural sunlight condition. We note that oxidation processes are controlled by many factors (e.g., pH, initial Mn^{2+} concentration, dissolved oxygen concentration, temperature, and solution chemistry, etc.). Nevertheless, the comparison of oxidation rates in Figure 5

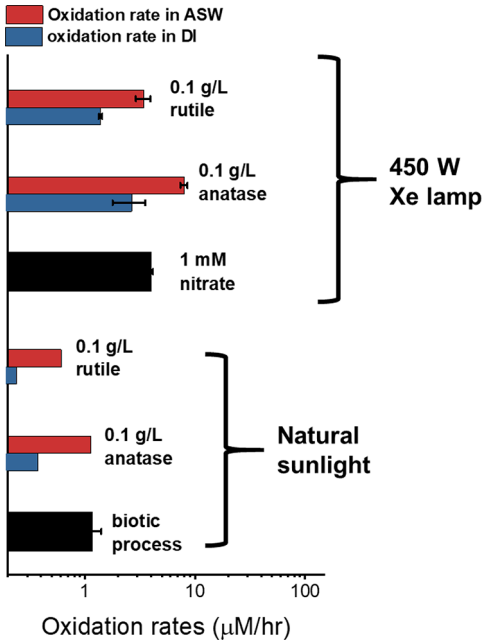

Figure 5. Comparison of the photocatalytic oxidation rates of Mn^{2+}(aq) in this study (using Xe lamp or calculated to natural sunlight condition) with previously reported oxidation rates in the presence of nitrate or via biotic processes.

provides an initial comparison of the relative importance of different oxidation pathways. As shown in the experimental and calculated results with TiO_2 (Figure 5), the calculated oxidation rates under natural sunlight condition are comparable to or faster than that of microbial oxidation processes. Natural semiconducting minerals occur in a wide variety of natural systems. Besides TiO_2 and Fe oxides, other natural semiconducting minerals such as ZnS and FeS, etc. may also serve to photocatalytically oxidize Mn^{2+}(aq), though different mineral catalysts might insert different photocatalytic oxidation mechanisms.

Our findings highlight the importance of a previously overlooked pathway: the photocatalytic oxidation of Mn^{2+}(aq), which might significantly contribute to Mn redox balance in nature. Meanwhile, the observed fast photocatalytic oxidation of Mn^{2+}(aq) raises the potential concern of semiconducting nanoparticles in influencing environmental redox systems. Through anthropogenic activities, TiO_2 and other semiconducting nanoparticles are released to a wide variety of environmental systems. On the basis of the observed rapid photocatalytic oxidation by TiO_2, accumulation of photoactive nanoparticles in nature might influence the balance of Mn redox. As an example of such anthropogenic impact, a recent study reported the occurrence of elevated concentration of dissolved Mn from the reduction of natural Mn oxides by emerging contaminants and fertilizers in U.S. groundwater, impacting more than 2.6 million people consuming the Mn contaminated groundwater.[83] The increase of semiconducting nanoparticles in environmental systems might promote the oxidation of Mn^{2+}(aq) and formation of Mn oxides, thus affecting the fate and transport of many other elements and contaminants. For example, Mn oxides are known to oxidize the more mobile As(III) into the less mobile As(V) species, whereas they can oxidize the less mobile Cr(III) species into more mobile and toxic Cr(VI) species.[3,84−87]

This study also demonstrates the direct formation of todorokite through heterogeneous nucleation on the surface of natural minerals under circumneutral conditions in the presence of large cations. To our knowledge, this is the first observation of direct formation of todorokite in laboratory settings under environmentally relevant conditions (Table S5). The results suggest that environmental conditions, such as solution chemistry and mineral surface, may govern the polymorphism of natural Mn oxides, and the latter in turn might potentially serve as a fingerprint to trace environmental conditions at the time of Mn oxide formation.

■ ASSOCIATED CONTENT

Supporting Information

The Supporting Information is available free of charge at https://pubs.acs.org/doi/10.1021/acsearthspacechem.1c00154.

XANES and EXAFS data and analyses, the calculation of quantum yields and the analyses of photocatalytic oxidation rates (PDF)

■ AUTHOR INFORMATION

Corresponding Author

Yuanzhi Tang − *School of Earth and Atmospheric Sciences, Georgia Institute of Technology, Atlanta, Georgia 30332-0340, United States;* orcid.org/0000-0002-7741-8646; Phone: (1) 404-894-3814; Email: yuanzhi.tang@eas.gatech.edu

Authors

Haesung Jung − *School of Earth and Atmospheric Sciences, Georgia Institute of Technology, Atlanta, Georgia 30332-0340, United States; School of Civil, Environmental and Chemical Engineering, Changwon National University, Changwon, Gyeongsangnam-do 51140, Republic of Korea;* orcid.org/0000-0002-8795-248X

Colin Snyder − *School of Earth and Atmospheric Sciences, Georgia Institute of Technology, Atlanta, Georgia 30332-0340, United States*

Wenqian Xu − *X-ray Science Division, Advanced Photon Source, Argonne National Laboratory, Lemont, Illinois 60439, United States*

Ke Wen − *Department of Ecosystem Science and Management, University of Wyoming, Laramie, Wyoming 82071, United States;* orcid.org/0000-0002-2080-6541

Mengqiang Zhu − *Department of Ecosystem Science and Management, University of Wyoming, Laramie, Wyoming 82071, United States;* orcid.org/0000-0003-1739-1055

https://doi.org/10.1021/acsearthspacechem.1c00154
ACS Earth Space Chem. 2021, 5, 2105−2114

Yan Li − *Beijing Key Laboratory of Mineral Environmental Function, School of Earth and Space Sciences, Peking University, Beijing 100871, China*
Anhuai Lu − *Beijing Key Laboratory of Mineral Environmental Function, School of Earth and Space Sciences, Peking University, Beijing 100871, China*

Complete contact information is available at: https://pubs.acs.org/10.1021/acsearthspacechem.1c00154

Notes

The authors declare no competing financial interest.

■ ACKNOWLEDGMENTS

This work is supported by U.S. National Science Foundation under Grant No. 1710285 (Y.T.). H.J. acknowledges support by the National Research Foundation of Korea (NRF) (Grant No. 2021R1F1A1063426) . A.L acknowledges support by Natural Science Foundation of China (Grants No. 91851208 and 41820104003) and the DDE-IUGS Big Science Program. We thank beamline scientists at Beamlines 17-BM-B and 12-BM-B at Advanced Photon Source (APS), 4-1 at Stanford Synchrotron Radiation Lightsource (SSRL), and 6-BM at National Synchrotron Radiation Lightsource-II (NSLS-II). Use of APS, SSRL, and NSLS-II are supported by the U.S. Department of Energy, Office of Science, Office of Basic Energy Sciences, under Contract Nos. DE-AC02-06CH11357, DE-AC02-76SF00515, and DE-SC0012704, respectively.

■ REFERENCES

(1) Sunda, W. G.; Kieber, D. J. Oxidation of humic substances by manganese oxides yields low-molecular-weight organic substrates. *Nature* **1994**, *367* (6458), 62−64.
(2) Stone, A. T.; Morgan, J. J. Reduction and dissolution of manganese (III) and manganese (IV) oxides by organics: 2. Survey of the reactivity of organics. *Environ. Sci. Technol.* **1984**, *18* (8), 617−624.
(3) Fendorf, S. E.; Zasoski, R. J. Chromium(III) oxidation by d-manganese oxide (MnO_2). 1. Characterization. *Environ. Sci. Technol.* **1992**, *26* (1), 79−85.
(4) Murray, K. J.; Webb, S. M.; Bargar, J. R.; Tebo, B. M. Indirect oxidation of Co (II) in the presence of the marine Mn (II)-oxidizing bacterium Bacillus sp. strain SG-1. *Appl. Environ. Microbiol.* **2007**, *73* (21), 6905−6909.
(5) Nealson, K. H.; Saffarini, D. Iron and manganese in anaerobic respiration: environmental significance, physiology, and regulation. *Annu. Rev. Microbiol.* **1994**, *48* (1), 311−343.
(6) Lefkowitz, J. P.; Rouff, A. A.; Elzinga, E. J. Influence of pH on the Reductive Transformation of Birnessite by Aqueous Mn(II). *Environ. Sci. Technol.* **2013**, *47* (18), 10364−10371.
(7) Wang, Z.; Xiong, W.; Tebo, B. M.; Giammar, D. E. Oxidative UO_2 Dissolution Induced by Soluble Mn (III). *Environ. Sci. Technol.* **2014**, *48* (1), 289−298.
(8) Wang, Z.; Tebo, B. M.; Giammar, D. E. Effects of Mn (II) on UO_2 Dissolution under Anoxic and Oxic Conditions. *Environ. Sci. Technol.* **2014**, *48* (10), 5546−5554.
(9) Elzinga, E. J. 54Mn Radiotracers Demonstrate Continuous Dissolution and Reprecipitation of Vernadite (δ-MnO_2) during Interaction with Aqueous Mn(II). *Environ. Sci. Technol.* **2016**, *50* (16), 8670−8677.
(10) Borch, T.; Kretzschmar, R.; Kappler, A.; Cappellen, P. V.; Ginder-Vogel, M.; Voegelin, A.; Campbell, K. Biogeochemical redox processes and their impact on contaminant dynamics. *Environ. Sci. Technol.* **2010**, *44* (1), 15−23.
(11) Villalobos, M.; Toner, B.; Bargar, J.; Sposito, G. Characterization of the manganese oxide produced by Pseudomonas putida strain MnB1. *Geochim. Cosmochim. Acta* **2003**, *67* (14), 2649−2662.
(12) Zhao, S.; Wang, Q.; Sun, J.; Borkiewicz, O. J.; Huang, R.; Saad, E. M.; Fields, B.; Chen, S.; Zhu, M.; Tang, Y. Effect of Zn coprecipitation on the structure of layered Mn oxides. *Chem. Geol.* **2018**, *493* (20), 234−245.
(13) Planavsky, N. J.; Asael, D.; Hofmann, A.; Reinhard, C. T.; Lalonde, S. V.; Knudsen, A.; Wang, X.; Ossa Ossa, F.; Pecoits, E.; Smith, A. J. B.; Beukes, N. J.; Bekker, A.; Johnson, T. M.; Konhauser, K. O.; Lyons, T. W.; Rouxel, O. J. Evidence for oxygenic photosynthesis half a billion years before the Great Oxidation Event. *Nat. Geosci.* **2014**, *7* (4), 283−286.
(14) Daye, M.; Klepac-Ceraj, V.; Pajusalu, M.; Rowland, S.; Farrell-Sherman, A.; Beukes, N.; Tamura, N.; Fournier, G.; Bosak, T. Light-driven anaerobic microbial oxidation of manganese. *Nature* **2019**, *576* (7786), 311−314.
(15) Lingappa, U. F.; Monteverde, D. R.; Magyar, J. S.; Valentine, J. S.; Fischer, W. W. How manganese empowered life with dioxygen (and vice versa). *Free Radical Biol. Med.* **2019**, *140*, 113−125.
(16) Lanza, N. L.; Wiens, R. C.; Arvidson, R. E.; Clark, B. C.; Fischer, W. W.; Gellert, R.; Grotzinger, J. P.; Hurowitz, J. A.; McLennan, S. M.; Morris, R. V.; Rice, M. S.; Bell III, J. F.; Berger, J. A.; Blaney, D. L.; Bridges, N. T.; Calef III, F.; Campbell, J. L.; Clegg, S. M.; Cousin, A.; Edgett, K. S.; Fabre, C.; Fisk, M. R.; Forni, O.; Frydenvang, J.; Hardy, K. R.; Hardgrove, C.; Johnson, J. R.; Lasue, J.; Le Mouélic, S.; Malin, M. C.; Mangold, N.; Martìn-Torres, J.; Maurice, S.; McBride, M. J.; Ming, D. W.; Newsom, H. E.; Ollila, A. M.; Sautter, V.; Schröder, S.; Thompson, L. M.; Treiman, A. H.; Van Bommel, S.; Vaniman, D. T.; Zorzano, M.-P. Oxidation of manganese in an ancient aquifer, Kimberley formation, Gale crater, Mars. *Geophys. Res. Lett.* **2016**, *43* (14), 7398−7407.
(17) Wang, Y.; Benkaddour, S.; Marafatto, F. F.; Peña, J. Diffusion- and pH-Dependent Reactivity of Layer-Type MnO2: Reactions at Particle Edges versus Vacancy Sites. *Environ. Sci. Technol.* **2018**, *52* (6), 3476−3485.
(18) Droz, B.; Dumas, N.; Duckworth, O. W.; Peña, J. A Comparison of the Sorption Reactivity of Bacteriogenic and Mycogenic Mn Oxide Nanoparticles. *Environ. Sci. Technol.* **2015**, *49* (7), 4200−4208.
(19) Remucal, C. K.; Ginder-Vogel, M. A critical review of the reactivity of manganese oxides with organic contaminants. *Environ. Sci.: Process. Impacts* **2014**, *16* (6), 1247−1266.
(20) Balgooyen, S.; Alaimo, P. J.; Remucal, C. K.; Ginder-Vogel, M. Structural transformation of MnO_2 during the oxidation of bisphenol A. *Environ. Sci. Technol.* **2017**, *51* (11), 6053−6062.
(21) Balgooyen, S.; Campagnola, G.; Remucal, C. K.; Ginder-Vogel, M. Impact of bisphenol A influent concentration and reaction time on MnO2 transformation in a stirred flow reactor. *Environ. Sci.: Process. Impacts* **2019**, *21* (1), 19−27.
(22) Kim, T.; Logan, B. E.; Gorski, C. A. A pH-Gradient Flow Cell for Converting Waste CO2 into Electricity. *Environ. Sci. Technol. Lett.* **2017**, *4* (2), 49−53.
(23) Fortunato, J.; Peña, J.; Benkaddour, S.; Zhang, H.; Huang, J.; Zhu, M.; Logan, B. E.; Gorski, C. A. Surveying Manganese Oxides as Electrode Materials for Harnessing Salinity Gradient Energy. *Environ. Sci. Technol.* **2020**, *54*, 5746−5754.
(24) Charbonnet, J. A.; Duan, Y.; van Genuchten, C. M.; Sedlak, D. L. Chemical Regeneration of Manganese Oxide-Coated Sand for Oxidation of Organic Stormwater Contaminants. *Environ. Sci. Technol.* **2018**, *52*, 10728−10736.
(25) Grebel, J. E.; Charbonnet, J. A.; Sedlak, D. L. Oxidation of organic contaminants by manganese oxide geomedia for passive urban stormwater treatment systems. *Water Res.* **2016**, *88*, 481−491.
(26) Huang, J.; Zhong, S.; Dai, Y.; Liu, C.-C.; Zhang, H. J. Effect of MnO_2 phase structure on the oxidative reactivity toward contaminant degradation. *Environ. Sci. Technol.* **2018**, *52*, 11309−11318.
(27) Zhao, S.; Li, C.; Liu, P.; Huang, R.; Saad, E.; Tang, Y. Zinc Presence during Mineral Formation Affects the Sorptive Reactivity of Manganese Oxide. *Soil Syst.* **2018**, *2* (2), 19.
(28) van Genuchten, C. M.; Pena, J. Sorption selectivity of birnessite particle edges: a d-PDF analysis of Cd(ii) and Pb(ii) sorption by

[small delta]-MnO2 and ferrihydrite. *Environ. Sci.: Process. Impacts* **2016**, *18* (8), 1030−1041.
(29) Diem, D.; Stumm, W. Is dissolved Mn^{2+} being oxidized by O_2 in absence of Mn-bacteria or surface catalysts? *Geochim. Cosmochim. Acta* **1984**, *48* (7), 1571−1573.
(30) Morgan, J. J. Kinetics of reaction between O_2 and Mn (II) species in aqueous solutions. *Geochim. Cosmochim. Acta* **2005**, *69* (1), 35−48.
(31) Wehrli, B.; Friedl, G.; Manceau, A. Reaction rates and products of manganese oxidation at the sediment-water interface. In *Aquatic Chemistry: Interfacial and Interspecies Processes*; Huang, C. P., Omelia, C. R., Morgan, J. J., Eds.; American Chemical Society, 1995; Vol. *244*, pp 111−134. DOI: 10.1021/ba-1995-0244.ch005.
(32) Johnson, C.; Ulrich, M.; Sigg, L.; Imboden, D. A mathematical model of the manganese cycle in a seasonally anoxic lake. *Limnol. Oceanogr.* **1991**, *36* (7), 1415−1426.
(33) Tebo, B. M.; Emerson, S. Effect of oxygen tension, Mn (II) concentration, and temperature on the microbially catalyzed Mn (II) oxidation rate in a marine fjord. *Appl. Environ. Microbiol.* **1985**, *50* (5), 1268−1273.
(34) Vojak, P. W.; Edwards, C.; Jones, M. V. Evidence for microbiological manganese oxidation in the River Tamar estuary, South West England. *Estuarine, Coastal Shelf Sci.* **1985**, *20* (6), 661−671.
(35) Nico, P. S.; Anastasio, C.; Zasoski, R. J. Rapid photo-oxidation of Mn (II) mediated by humic substances. *Geochim. Cosmochim. Acta* **2002**, *66* (23), 4047−4056.
(36) Jung, H.; Chadha, T.; Kim, D.; Biswas, P.; Jun, Y.-S. Photochemically-assisted Fast Abiotic Oxidation of Manganese and Formation of δ-MnO_2 Nanosheets in Nitrate Solution. *Chem. Commun.* **2017**, *53*, 4445−4448.
(37) Learman, D.; Wankel, S.; Webb, S.; Martinez, N.; Madden, A.; Hansel, C. Coupled biotic-abiotic Mn (II) oxidation pathway mediates the formation and structural evolution of biogenic Mn oxides. *Geochim. Cosmochim. Acta* **2011**, *75* (20), 6048−6063.
(38) Jung, H.; Chadha, T. S.; Min, Y.; Biswas, P.; Jun, Y.-S. Photochemically-assisted Synthesis of Birnessite Nanosheets and Their Structural Alteration in the Presence of Pyrophosphate. *ACS Sustainable Chem. Eng.* **2017**, *5* (11), 10624−10632.
(39) Zhang, T.; Liu, L.; Tan, W.; Suib, S. L.; Qiu, G.; Liu, F. Photochemical Formation and Transformation of Birnessite: Effects of Cations on Micromorphology and Crystal Structure. *Environ. Sci. Technol.* **2018**, *52* (12), 6864−6871.
(40) Post, J. E. Manganese oxide minerals: Crystal structures and economic and environmental significance. *Proc. Natl. Acad. Sci. U. S. A.* **1999**, *96* (7), 3447−3454.
(41) Feng, X. H.; Zhu, M.; Ginder-Vogel, M.; Ni, C.; Parikh, S. J.; Sparks, D. L. Formation of nano-crystalline todorokite from biogenic Mn oxides. *Geochim. Cosmochim. Acta* **2010**, *74* (11), 3232−3245.
(42) Atkins, A. L.; Shaw, S.; Peacock, C. L. Release of Ni from birnessite during transformation of birnessite to todorokite: Implications for Ni cycling in marine sediments. *Geochim. Cosmochim. Acta* **2016**, *189*, 158−183.
(43) Yang, P.; Lee, S.; Post, J. E.; Xu, H.; Wang, Q.; Xu, W.; Zhu, M. Trivalent manganese on vacancies triggers rapid transformation of layered to tunneled manganese oxides (TMOs): Implications for occurrence of TMOs in low-temperature environment. *Geochim. Cosmochim. Acta* **2018**, *240*, 173−190.
(44) Feng, X.; Zhao, H.; Liu, F.; Cui, H.; Tan, W.; Li, W. Transformation from Phyllomanganates to Todorokite under Various Conditions: A Review of Implication for Formation Pathway of Natural Todorokite. *Advances in the Environmental Biogeochemistry of Manganese Oxides*; American Chemical Society, 2015; Vol. *1197*, pp 107−134. DOI: 10.1021/bk-2015-1197.ch006
(45) Jung, H.; Taillefert, M.; Sun, J.; Wang, Q.; Borkiewicz, O. J.; Liu, P.; Yang, L.; Chen, S.; Chen, H.; Tang, Y. Redox Cycling Driven Transformation of Layered Manganese Oxides to Tunnel Structures. *J. Am. Chem. Soc.* **2020**, *142* (5), 2506−2513.
(46) Li, Y.; Ding, C.; Liu, Y.; Li, Y.; Lu, A.; Wang, C.; Ding, H. Visible Light Photocatalysis of Natural Semiconducting Minerals. In *Advances in Photocatalytic Disinfection*; An, T., Zhao, H., Wong, P. K., Eds.; Springer: Berlin, Heidelberg, 2017; pp 17−39. DOI: 10.1007/978-3-662-53496-0_2
(47) Lu, A.; Li, Y.; Ding, H.; Xu, X.; Li, Y.; Ren, G.; Liang, J.; Liu, Y.; Hong, H.; Chen, N.; Chu, S.; Liu, F.; Li, Y.; Wang, H.; Ding, C.; Wang, C.; Lai, Y.; Liu, J.; Dick, J.; Liu, K.; Hochella, M. F. Photoelectric conversion on Earth's surface via widespread Fe- and Mn-mineral coatings. *Proc. Natl. Acad. Sci. U. S. A.* **2019**, *116* (20), 9741−9746.
(48) Xu, X.; Li, Y.; Li, Y.; Lu, A.; Qiao, R.; Liu, K.; Ding, H.; Wang, C. Characteristics of desert varnish from nanometer to micrometer scale: A photo-oxidation model on its formation. *Chem. Geol.* **2019**, *522*, 55−70.
(49) Meinhold, G. Rutile and its applications in earth sciences. *Earth-Sci. Rev.* **2010**, *102* (1−2), 1−28.
(50) Ranade, M. R.; Navrotsky, A.; Zhang, H. Z.; Banfield, J. F.; Elder, S. H.; Zaban, A.; Borse, P. H.; Kulkarni, S. K.; Doran, G. S.; Whitfield, H. J. Energetics of nanocrystalline TiO2. *Proc. Natl. Acad. Sci. U. S. A.* **2002**, *99*, 6476−6481.
(51) Hoffmann, M. R.; Martin, S. T.; Choi, W.; Bahnemann, D. W. Environmental Applications of Semiconductor Photocatalysis. *Chem. Rev.* **1995**, *95* (1), 69−96.
(52) Loeb, S. K.; Alvarez, P. J. J.; Brame, J. A.; Cates, E. L.; Choi, W.; Crittenden, J.; Dionysiou, D. D.; Li, Q.; Li-Puma, G.; Quan, X.; Sedlak, D. L.; David Waite, T.; Westerhoff, P.; Kim, J.-H. The Technology Horizon for Photocatalytic Water Treatment: Sunrise or Sunset? *Environ. Sci. Technol.* **2019**, *53*, 2937−2947.
(53) He, X.; Hwang, H.-M. Engineered TiO_2 Nanoparticles: Their Fate and Effects in Natural Aquatic Environments. *Chem. Phys. Res. J.* **2014**, *7*, 1−20.
(54) Rodríguez-Romero, A.; Ruiz-Gutiérrez, G.; Viguri, J. R.; Tovar-Sánchez, A. Sunscreens as a New Source of Metals and Nutrients to Coastal Waters. *Environ. Sci. Technol.* **2019**, *53* (17), 10177−10187.
(55) Weir, A.; Westerhoff, P.; Fabricius, L.; Hristovski, K.; von Goetz, N. Titanium Dioxide Nanoparticles in Food and Personal Care Products. *Environ. Sci. Technol.* **2012**, *46* (4), 2242−2250.
(56) Westerhoff, P.; Song, G.; Hristovski, K.; Kiser, M. A. Occurrence and removal of titanium at full scale wastewater treatment plants: implications for TiO2 nanomaterials. *J. Environ. Monit.* **2011**, *13* (5), 1195−1203.
(57) Neal, C.; Jarvie, H.; Rowland, P.; Lawler, A.; Sleep, D.; Scholefield, P. Titanium in UK rural, agricultural and urban/industrial rivers: Geogenic and anthropogenic colloidal/sub-colloidal sources and the significance of within-river retention. *Sci. Total Environ.* **2011**, *409* (10), 1843−1853.
(58) Montserrat, F.; Renforth, P.; Hartmann, J.; Leermakers, M.; Knops, P.; Meysman, F. J. R. Olivine Dissolution in Seawater: Implications for CO2 Sequestration through Enhanced Weathering in Coastal Environments. *Environ. Sci. Technol.* **2017**, *51* (7), 3960−3972.
(59) Tebo, B. M.; Clement, B. G.; Dick, G. J. Biotransformations of manganese. *Manual of Environmental Microbiology*, 3rd ed.; ASM Press, 2007; pp 1223−1238.
(60) Davies, S. H.; Morgan, J. J. Manganese (II) oxidation kinetics on metal oxide surfaces. *J. Colloid Interface Sci.* **1989**, *129* (1), 63−77.
(61) Junta, J. L.; Hochella Jr, M. F. Manganese (II) oxidation at mineral surfaces: A microscopic and spectroscopic study. *Geochim. Cosmochim. Acta* **1994**, *58* (22), 4985−4999.
(62) Cerrato, J. M.; Hochella Jr, M. F.; Knocke, W. R.; Dietrich, A. M.; Cromer, T. F. Use of XPS to identify the oxidation state of Mn in solid surfaces of filtration media oxide samples from drinking water treatment plants. *Environ. Sci. Technol.* **2010**, *44* (15), 5881−5886.
(63) Cerrato, J. M.; Knocke, W. R.; Hochella, M. F.; Dietrich, A. M.; Jones, A.; Cromer, T. F. Application of XPS and Solution Chemistry Analyses to Investigate Soluble Manganese Removal by MnOx(s)-Coated Media. *Environ. Sci. Technol.* **2011**, *45* (23), 10068−10074.

(64) Webb, S. M. SIXPack a Graphical User Interface for XAS Analysis Using IFEFFIT. *Phys. Scr.* **2005**, *T115*, 1011−1014.
(65) Ravel, B.; Newville, M. ATHENA, ARTEMIS, HEPHAESTUS: data analysis for X-ray absorption spectroscopy using IFEFFIT. *J. Synchrotron Radiat.* **2005**, *12* (4), 537−541.
(66) Manceau, A.; Marcus, M. A.; Grangeon, S. Determination of Mn valence states in mixed-valent manganates by XANES spectroscopy. *Am. Mineral.* **2012**, *97* (5−6), 816−827.
(67) Hansel, C. M.; Francis, C. A. Coupled photochemical and enzymatic Mn (II) oxidation pathways of a planktonic Roseobacter-like bacterium. *Appl. Environ. Microbiol.* **2006**, *72* (5), 3543−3549.
(68) Learman, D.; Voelker, B.; Vazquez-Rodriguez, A.; Hansel, C. Formation of manganese oxides by bacterially generated superoxide. *Nat. Geosci.* **2011**, *4* (2), 95−98.
(69) Francis, C. A.; Co, E.-M.; Tebo, B. M. Enzymatic manganese-(II) oxidation by a marine α-proteobacterium. *Appl. Environ. Microbiol.* **2001**, *67* (9), 4024−4029.
(70) Yang, Y.; Chen, B.; Hower, J.; Schindler, M.; Winkler, C.; Brandt, J.; Di Giulio, R.; Ge, J.; Liu, M.; Fu, Y.; Zhang, L.; Chen, Y.; Priya, S.; Hochella, M. F. Discovery and ramifications of incidental Magnéli phase generation and release from industrial coal-burning. *Nat. Commun.* **2017**, *8* (1), 194.
(71) Yuan, Y.; He, K.; Byles, B. W.; Liu, C.; Amine, K.; Lu, J.; Pomerantseva, E.; Shahbazian-Yassar, R. Deciphering the Atomic Patterns Leading to MnO2 Polymorphism. *Chem.* **2019**, *5* (7), 1793−1805.
(72) Toyoda, K.; Tebo, B. M. Kinetics of Mn(II) oxidation by spores of the marine Bacillus sp. SG-1. *Geochim. Cosmochim. Acta* **2016**, *189*, 58−69.
(73) Soldatova, A. V.; Balakrishnan, G.; Oyerinde, O. F.; Romano, C. A.; Tebo, B. M.; Spiro, T. G. Biogenic and Synthetic MnO_2 Nanoparticles: Size and Growth Probed with Absorption and Raman Spectroscopies and Dynamic Light Scattering. *Environ. Sci. Technol.* **2019**, *53* (8), 4185−4197.
(74) Spiro, T. G.; Bargar, J. R.; Sposito, G.; Tebo, B. M. Bacteriogenic manganese oxides. *Acc. Chem. Res.* **2010**, *43* (1), 2−9.
(75) Lee, S.; Xu, H. XRD and TEM studies on nanophase manganese oxides in freshwater ferromanganese nodules from Green Bay, Lake Michigan. *Clays Clay Miner.* **2016**, *64* (5), 523−536.
(76) Webb, S.; Tebo, B.; Bargar, J. Structural characterization of biogenic Mn oxides produced in seawater by the marine Bacillus sp. strain SG-1. *Am. Mineral.* **2005**, *90* (8−9), 1342−1357.
(77) Santelli, C. M.; Webb, S. M.; Dohnalkova, A. C.; Hansel, C. M. Diversity of Mn oxides produced by Mn (II)-oxidizing fungi. *Geochim. Cosmochim. Acta* **2011**, *75* (10), 2762−2776.
(78) Webb, S.; Fuller, C.; Tebo, B.; Bargar, J. Determination of uranyl incorporation into biogenic manganese oxides using X-ray absorption spectroscopy and scattering. *Environ. Sci. Technol.* **2006**, *40* (3), 771−777.
(79) Feng, X. H.; Tan, W. F.; Liu, F.; Wang, J. B.; Ruan, H. D. Synthesis of todorokite at atmospheric pressure. *Chem. Mater.* **2004**, *16* (22), 4330−4336.
(80) Atkins, A. L.; Shaw, S.; Peacock, C. L. Nucleation and growth of todorokite from birnessite: Implications for trace-metal cycling in marine sediments. *Geochim. Cosmochim. Acta* **2014**, *144*, 109−125.
(81) Hu, X.; Kitchaev, D. A.; Wu, L.; Zhang, B.; Meng, Q.; Poyraz, A. S.; Marschilok, A. C.; Takeuchi, E. S.; Takeuchi, K. J.; Ceder, G.; Zhu, Y. Revealing and Rationalizing the Rich Polytypism of Todorokite MnO2. *J. Am. Chem. Soc.* **2018**, *140* (22), 6961−6968.
(82) Ilton, E. S.; Post, J. E.; Heaney, P. J.; Ling, F. T.; Kerisit, S. N. XPS Determination of Mn Oxidation States in Mn (Hydr) oxides. *Appl. Surf. Sci.* **2016**, *366*, 475−485.
(83) McMahon, P. B.; Belitz, K.; Reddy, J. E.; Johnson, T. D. Elevated Manganese Concentrations in United States Groundwater, Role of Land Surface-Soil-Aquifer Connections. *Environ. Sci. Technol.* **2019**, *53* (1), 29−38.
(84) Manning, B. A.; Fendorf, S. E.; Bostick, B.; Suarez, D. L. Arsenic (III) oxidation and arsenic (V) adsorption reactions on synthetic birnessite. *Environ. Sci. Technol.* **2002**, *36* (5), 976−981.
(85) Villalobos, M.; Escobar-Quiroz, I. N.; Salazar-Camacho, C. The influence of particle size and structure on the sorption and oxidation behavior of birnessite: I. Adsorption of As(V) and oxidation of As(III). *Geochim. Cosmochim. Acta* **2014**, *125*, 564−581.
(86) Tang, Y.; Webb, S. M.; Estes, E. R.; Hansel, C. M. Chromium(iii) oxidation by biogenic manganese oxides with varying structural ripening. *Environ. Sci.: Process. Impacts* **2014**, *16* (9), 2127−2136.
(87) Landrot, G.; Ginder-Vogel, M.; Livi, K.; Fitts, J. P.; Sparks, D. L. Chromium (III) oxidation by three poorly-crystalline manganese (IV) oxides. 1. Chromium (III)-oxidizing capacity. *Environ. Sci. Technol.* **2012**, *46* (21), 11594−11600.

https://doi.org/10.1021/acsearthspacechem.1c00154
ACS Earth Space Chem. 2021, 5, 2105−2114